Macro- and micro-physical characteristics of different parts of mixed convective-stratiform clouds and differences in their responses to seeding

Dejun Li[1], Chuanfeng Zhao[2*], Peiren Li[3], Cao Liu[4], Dianli Gong[5], Siyao Liu[2], Zhengteng Yuan[1], Yingying Chen[1]

1 Hubei Meteorological Service Center, Wuhan, China 430205;

2 College of Global Change and Earth System Science, Beijing Normal University, Beijing, China 100875;

3 Weather Modification Office of Shanxi Province, Taiyuan, China 030032;

4 Wuhan Central Meteorological Observatory, Wuhan, China 430074;

5 Weather Modification Office of Shandong Province, Jinan, China 250031

Correspondence to: Chuanfeng Zhao, czhao@bnu.edu.cn

Submitted to: Advance in Atmospheric Sciences

Abstract: This study investigates the cloud macro- and micro-physical characteristics in the convective and stratiform regions and their different responses to the seeding for mixed convective-stratiform clouds occurred in Shandong province on 21 May 2018, based on the observations from the aircraft, the Suomi National Polar-Orbiting Partnership (NPP) satellite, and the high-resolution Himawari-8 (H8) satellite. The aircraft observations show that there are deeper convection and significantly enhanced radar echoes with higher tops in response to seeding in the convective region. This is linked with the conversion of supercooled liquid droplets to ice crystals with released latent heat, resulting in strengthened updrafts, enhanced radar echoes, higher cloud tops, and then more and larger precipitation particles. In contrast, in the stratiform cloud region, after the AgI seeding, the radar echoes become significantly weaker at heights close to the seeding layer, with the echo tops lowered by 1.4–1.7 km. In addition, a hollow structure appears at the height of 6.2–7.8 km with a depth of about 1.6 km and a diameter of about 5.5 km, and response features such as icing seeding tracks appear. These suggest that the transformation between droplets and ice particles was accelerated by the seeding in the stratiform part. The NPP and H8 satellites also show that convective activities are stronger in the convective region after seeding; while in the stratiform region, a cloud seeding track with a width of 1–3 km appears 10 km downstream of the seeding layer 15 minutes after the AgI seeding, which moves along the wind direction as width increases.

Keywords: Airborne Ka-band Precipitation Radar (KPR), mixed convective-stratiform clouds, convective region, stratiform region, cloud seeding, cloud microphysical properties

Highlights:

(1) More enhanced convective activities occur with higher cloud tops in response to seeding in convective cloud region.

(2) Dynamic seeding mechanism involves in the convective cloud region, resulting in more and larger precipitation particles.

(3) Conversion of liquid to ice particles is accelerated with weaker radar echoes around the seeding layer in stratiform cloud region.

https://doi.org/10.1007/s00376-022-2003-8

1. Introduction

Water is critical to human society and the natural environment. As water resources are limited, the continuously-increasing human demands have prompted considerable interests in the feasibility of increasing water supply through weather modification. To increase the precipitation, especially for arid and semi-arid regions, cold-cloud seeding experiments have been conducted since the 1940s (Smith, 1949; Langmuir 1950; Vonnegut et.al., 1971; Hobbs et al.1981; Bruintjes 1999; Dong et al., 2020). Because the AgI has similar crystal structure to ice (Vonnegut et.al., 1971), its particles can act as ice nuclei (IN) (DeMott, 1997). Thus, AgI has been widely used in the cloud seeding both on the ground and in the air. The seeding with AgI can increase both precipitation and snowfall, thus changing the equilibrium between the water supply and demand (Xue et. al., 2013a,2013b,2014; Boe et.al., 2014; Jing and Geerts, 2015; Jing et.al., 2015,2016).

Since weather modification has been attempted, numerous studies have been conducted on the effects of cloud seeding experiments on the precipitation and cloud microphysical characteristics over target areas (Biondini et al., 1977; Nirel et.al., 1995; Gabriel, 1999; Silverman, 2001; Woodley et al., 2003a,2004; Pokharel et al., 2015; Yao, 2019). In recent years, with the application of airborne detection equipments, the cloud micro-physical characteristic (Lawson, et al., 2006,2008,2019; Yang et al., 2019; Zhao et al., 2019) and variation in cloud responses to seeding (Heymsfield et.al, 2011; Cai et.al., 2013; Dong et.al., 2020) can be more accurately analyzed. By using the Advanced Very High Resolution Radiometer (AVHRR) onboard the National Oceanic and Atmospheric Administration (NOAA) polar orbiting satellites, Rosenfeld et.al. (2005) observed a cloud seeding track formed after seeding, with a duration of 38 minutes. Through the ground-based X-band radar, the airborne W-band cloud radar and other aircraft instruments, French et.al. (2018) observed the process that the cloud seeding with AgI in super-cooled stratus causes the transformation of surrounding supercooled water into ice crystals, followed by the deposition of water vapor and the growth of ice crystals.

The studies mentioned above demonstrate that static seeding mechanism can play a significant role (Bruintjes, 1999). Under the humid, neutral or unstable atmospheric conditions, the release of latent heat due to the ice formation in clouds causes nearby air masses to gain buoyancy and further changes the flow field, resulting in deeper convective clouds, which was known as the dynamic seeding mechanism (Simpson et. al., 1971; Rosenfeld et. al., 1989). Scientists have studied the dynamic seeding mechanism with experiments mainly for summer convections (from cumulus to cumulonimbus clouds). However, due to the limitation of detection methods and the factors such as rapid formation and dissipation of convective clouds, it was challenging to trace the changes in macro- and micro-physical characteristics caused by the seeding of catalysts. Researchers have focused mostly on the changes of cloud-top height and surface precipitation but not on the detailed physical processes. Therefore, the dynamic seeding mechanism still lacks the verification through directly-observed facts (Sax et al., 1979; Hallet 1981; Woodley et al., 1982; Orville, 1996). Due to the complex structural characteristics of mixed convective-stratiform clouds (Lawson et.al., 2015; Lin et.al., 2019), there have been few studies related to the response of different cloud parts after seeding, such as the convective and stratiform parts, as well as the presence or absence of dynamic seeding effects.

In 2014, the University of Wyoming developed the airborne Ka-band precipitation cloud radar (KPR), which is well known for its high spatio-temporal resolution with 0.1–20 μs sampling time resolution and 30 m spatial resolution. This radar provides direct observation of cloud property responses to seeding in the context of both macro- and micro-physical characteristics (Heymsfield et. al., 2013; Pazmany et al., 2018). In addition, the Suomi National Polar-Orbiting Partnership (NPP) satellite in 2011 and the Himawari-8 (H8) satellite in 2014 were successfully launched successively, and the resolution of thermal infrared bands of the NPP/ VIIRS (Visible Infrared Imaging Radiometer Suite Sensor) has been improved by a factor of 3 compared with sensors such as the Moderate Resolution Imaging Spectroradiometer (MODIS), providing unique advantages in accurately resolving small convective clouds during their initial/developing stages, and also in monitoring the cloud track (Hillger et al., 2013; Rosenfeld et al., 2014). In this study, to our best knowledge, for the first time in China, we use the airborne KPR to monitor the evolution characteristics of radar echoes before and after the seeding for a spring mixed convective-stratiform cloud occurred in Shandong Province on 21 May 2018. Moreover, we combine the satellite observations and other data to comprehensively analyze the cloud characteristics in the stratiform region and the role of possible dynamic seeding mechanism in the convective region.

The remainder of this paper was organized as follows. The data sources used are introduced in section 2. Section 3 presents the synoptic situation and experiment overview. Section 4 shows the main results of this study. A conceptual model of seeding at different parts of mixed convective-stratiform clouds was proposed in section 5. Finally, the conclusions and discussion are given in section 6.

2. Data

The data used in this study are obtained from aircraft, satellite and ground observations. The experiment area for cloud detection and seeding was the region bounded by 117°E–119°E, 36.5°N–37.5°N. The ground observations include the synoptic meteorological observation data in Shandong Province and 6-minute S-band Doppler weather radar data from Binzhou in Shandong on 21 May 2018. Here, the airborne data and satellite data are described.

2.1 Airborne data

The KingAir aircraft was used for the cloud seeding and observation. This aircraft is owned and operated by the Shanxi Province Weather Modification Office. The aircraft was equipped with instruments for measuring the cloud, precipitation and other meteorological elements, including the airborne KPR, the particle size probes from Droplet Measurement Technologies (DMT) and 20 Hz Aircraft-Integrated Meteorological Measurement System

(AIMMS-20). It was also equipped with the Beidou satellite navigation and position system and a flare rack with positions for 24 flares, as shown in Fig. 1. The airborne KPR (ProSensing, USA) is the Ka-band precipitation cloud radar, which scans vertically, both upward and downward, and employs a data processing technique using the coherent power spectrum to reduce the noise. The Cloud Droplet Probe (CDP, DMT) based on forward-scattering theory, has 30 size bins, with a sampling frequency of 1 Hz, a measurement range of 2-50 μm with a resolution of 1-2 μm. It can measure particle number concentrations in the range of 0–1.0×10^{4} cm^{-3}, with the uncertainty of approximately 20% (Lance, 2012; Yang et. al, 2019; Yang et. al., 2020). The Cloud Imaging Probe (CIP, DMT) has 62 size bins, with a sampling frequency of 1 Hz, a measurement range of 25–1550 μm and a resolution of 25 μm. The Precipitation Imaging Probe (PIP, DMT) has the same number of size bins and sampling frequency as the CIP. However, the PIP has a measurement range of 100–6200 μm with a spectral resolution of 100 μm. The specifications for main instruments used in this study are listed in Table 1, including the measurement ranges, temporal resolution and the particle size spectral bin resolution. Note that both cloud and precipitation particle probes are calibrated in the ground laboratory before every flight.

2.2 Satellite data

The NPP VIIRS satellite observations at 05:25 UTC on 21 May 2018 are used in this study, which is provided to the public by the NOAA website (http://www.bou.class.noaa.gov/saa/products/welcome). It has five channels with central wavelengths at 0.64, 0.865, 1.615, 3.745 and 11.45 μm, with high spatial resolution of 375 m. When the NPP satellite passed by the study region at 05:25 UTC on 21 May 2018, the time gone away from the aicraft seeding and detection at A–B–C–D–E–F–G is about 33–28–27–16–15–6–6 minutes.

The 10-minute full-disc data from the H8 on 21 May provided by the Data Service website (http://www.bou.class.noaa.gov/saa/products/welcome) are also used in this study. The Advanced Himawari Imager (AHI, ftp://ftp.ptree.jaxa.jp) onboard the H8 completes each full-disc scan within 10 minutes, greatly facilitating the tracking of the developing cloud seeding tracks. The H8/AHI sensor has 16 channels ranging from 0.46 to 13.3 μm. Meanwhile, the spatial resolution of visible and near-infrared channels ranges from 0.5–1 km, and the spatial resolution of infrared channel is only 2 km.

3. Synoptic situation and experiment overview

3.1 Synoptic situation

Figure 2 shows that Shandong was dominated by westerly flow at 500 hPa at 00:00 UTC on 21 May 2018. There were two weak waves in the west successively moving eastward to affect Shandong. At 700 hPa, there was a warm shear around Shandong in the morning, causing the precipitation. Meanwhile, a significant cold shear near the Hetao region moved eastward and continued to affect Shandong, with the wind direction of 300° and wind speed of 11 $m \cdot s^{-1}$, resulting in the persistent precipitation in Shandong to the afternoon of the 21st. At the surface, Shandong was located at the back of the anticyclone circulation over the sea during 00:00–12:00 UTC on 21 May, dominated by the easterly wind. There was a surface convergence line near the flight track at that time, and the accumulated rainfall at regions near the flight track was 1–7 mm during 03:00–06:00 UTC.

3.2 Overview of the seeding and detection experiment

The flight track was over north-central Shandong Province, close to the northern edge of central Taishan Mountains (Fig. 3a). In addition, the flight altitude was 5300 m, the flight speed was 101–113 $m \cdot s^{-1}$, and the height of the freezing level was 4200 m. At 04:37 UTC, the aircraft was flying at the height of 1800 m over point O1, and the KPR began to make observations. At 04:45 UTC, the aircraft was circling over point O2 and ascended to 5300 m. During 04:52–05:19 UTC, the aircraft performed the seeding operation along the zigzagging path of A–B–C–D–E–F–G. At 04:52 UTC, 2 AgI flares were burned and released at 5300 m (1 on each side) simultaneously at point A, and totally four flares (2 on each side) were burned till 05:00 UTC. Note that the lasting time length for every flare is 5 minutes. Each flare consists of 27 g AgI, and the nucleation rate of AgI is 1.08×10^{15} per gram at -10℃. The AgI in each flare can effectively play the role of ice nucleus at temperature below -4℃. At 05:00 UTC, within the clouds with sufficient super-cooled water (abundant super-cooled water particularly within the convective core part about 1-2 km below the aircraft), the aircraft burned totally 8 AgI flares also at 5300 m (4 on each side) with 2 AgI flares (1 on each side) burned simultaneously at a given time. The aircraft finished the seeding operation at point G at 05:19 UTC. Note that short overlap time could exist between two adjacent flares, which could introduce some uncertainties to the quantitative response of cloud properties to seeding. Afterwards, it descended gradually from 5300 m to point I (2800 m) to conduct a backward detection experiment for the seeding effect. The seeding was carried out along three lines of the zigzagging flight track (A–G), with a seeding duration of 27 minutes and a seeding rate of $0.6 g \cdot s^{-1}$, consuming 972 g AgI (36 flares with 27 g for each). Note that different total amount of AgI flares have been released sometimes at two parts of clouds although the released AgI amount at a given time is roughly similar, which could affect the response of clouds to the seeding and make the quantitative comparison of cloud seeding effect at two locations challenging. To minimize this impact, we mainly analyze the differences in cloud seeding effect at two locations qualitatively while some quantitative results about the changes of cloud microphysical properties will also be provided.

The aircraft returned to the point O at 05:48 UTC. To compare and analyze the situation before the seeding and the backward detection results in detail, S1–S3 (04:54:30–04:55:30 UTC) and S4–S6 (05:01:22–05:02:22 UTC) are marked in Fig. 3a as the two periods of AgI seeding. The middle points of the two seeding periods are marked as S2 and S5, respectively. And the time nodes of the backward detection are determined based on the wind direction and speed at the seeding layer. The purple dashed line was the line segment between S2 and S5 moving at 11 $m \cdot s^{-1}$ along the wind direction of 300°. It intersects with the line segment G–H of the backward detection, with the crossover points marked as R5 and R2, respectively. Taking the two points R5 and R2 as middle points, respectively, the corresponding backward detection periods are determined as R4–R6 (05:26:25–05:27:25 UTC) and R1–R3 (05:24:25–05:25:25 UTC), respectively. Note that the magenta lines represent the parallel lines of system movement with winds for the period between forward and backward flight time.

The cloud macro-physical characteristics during the seeding operation were obtained 0–2 km above the cloud top. The temperature was between −5°C and −8°C, and the relative humidity was all about 100% (Fig. 3b). Note that at 04:37 UTC, a moderate-intensity turbulence occurred. The aircraft experienced light, moderate, and then severe icing, indicating that the super-cooled water content varied along the flight track.

Fig. 3c shows the cross-section of radar reflectivity along the aircraft flight track from 04:37 to 05:49 UTC measured by the ground radar at Binzhou. Section A–B (seen from Fig. 3b) of the zigzagging flight track was mostly covered with convective clouds, with convective centers at the height of 3–5 km and echo centers reaching above 30 dBZ at limited locations that are not clearly shown in Fig. 3c. Section C–D (seen from Fig. 3b) of the zigzagging flight track was mostly covered with stratiform clouds with radar echoes below 25 dBZ. In addition, convection was observed during period S1–S3 (within A–B), while more stratiform clouds were observed during period S4–S6 (within C–D) (Fig. 3c).

4. Analysis and Results

4.1 Evolution characteristics of airborne KPR echoes

During the two seeding periods of S1–S3 and S4–S6 as well as the corresponding backward detection periods of R4–R6 and R1–R3 (Fig. 3a), the evolution characteristics of the real-time radar echoes by the airborne KPR were analyzed (Fig. 4). From Figs. 3c and 4c, it can be seen that the mixed convective-stratiform cloud is the target object for seeding operation. The convective region and the stratiform region in the mixed convective-stratiform clouds were selected for the seeding during S1–S3 and S4–S6, respectively. In addition, a bright band (temperature around 0 ℃) can be found within the height of 4200–4300 m. By comparing Figs. 4a and 4b, it can be found that during S1–S3 the radar echoes in the convective region were significantly enhanced after the seeding. An echo center of 20–35 dBZ appeared at the height of 2–4 km, and the echo top became dense and was uplifted by 0.5–1.0 km. The differences between Figs. 4d and 4e show that the echoes became significantly weaker above the seeding layer (5200 m) after the seeding operation in the stratiform region during S4–S6, and an hollow structure of echoes appeared at the height of 6.2–7.8 km, with the largest depth reaching about 1.6 km and a diameter of about 5.5 km (calculated as follows: 05:24:30–05:25:20 UTC → 50 s × 110 $m \cdot s^{-1}$ = 5.5 km). The mechanism that the hollow structure forms will be discussed in section 5. In addition, the top of the hollow part was covered by a thin layer with echoes being −5 dBZ (Fig. 4e). By comparing Figs. 4a and 4b as well as Figs. 4d and 4e, it shows that the echoes were significantly enhanced at the height of 2–4 km at time 22–32 minutes after the seeding operation, with the enhancement amplitude exceeding 5 dBZ in all areas. In addition, a strong echo center of 35 dBZ appeared in the convective region.

Figure 5 shows the contoured frequency by altitude diagrams (CFADs) of the radar reflectivity *Ze* for the two seeding periods. The CFADs explain the joint probability distribution function of height and reflectivity and represent the frequency distribution in a coordinate system of reflectivity bins (x axis) and altitude (y axis). In each CFAD, the distribution was normalized by dividing the observed frequency by the maximum frequency for all height - reflectivity bins, to compare the CFADs among different cases. During S1–S3, the differences of the echoes in the convective region between before and after the seeding show that the echoes became stronger with a denser layer at heights within 3 km around (both above and below) the seeding layer, and the echo top height increased by 1–2 km. In addition, the median *Ze* was 5–7 dBZ larger than that before the seeding operation, and the echo near the surface increased to 28 dBZ from 12 dBZ (Figs. 5a and 5b). In contrast, Figs. 5c and 5d show that the echoes in the stratiform region got significantly weaker at heights within 2–3 km around (both above and below) the seeding layer after the seeding during S4–S6. In addition, the median *Ze* was 2–3 dBZ lower than that before the seeding, and the echo top height decreased by 1.4–1.7 km. Before the seeding operation, the median *Ze* reached the peak of 21.2 dBZ at the height of 3.5 km, and the *Ze* decreased with increasing height above this level while decreased with decreasing height below this level, falling to 9 dBZ at the surface. During the period R1–R3, the variation trend of the Ze median value was similar to that before the seeding. However, the peak Ze value of 19.7 dBZ appeared at about 2.1 km, and Ze was about 8.5 dBZ near the surface, which were both smaller than those before the seeding. We would like to mention that natural evolution could also play some roles to the variation of cloud properties indicated here and other places over seeded area, which are difficult to separate and further discussed later in discussion section.

Figure 6 shows the CFADs of the Doppler radar velocity, with the same analysis method as shown in Fig. 5. The range of Doppler radar velocity widens after the seeding. Specifically, the velocity changes from 3–5 $m \cdot s^{-1}$ to 5–8 $m \cdot s^{-1}$ in the convective region, and from 3–5 $m \cdot s^{-1}$ to 4–7 $m \cdot s^{-1}$ in the stratiform region. Besides, the median, 25th and 75th percentiles of the Doppler radar velocity are very close to each other before the seeding, but after the seeding, the intervals between them distinctly increase. This implies that the micro-physical processes play a role. After the seeding operation, the AgI was rapidly nucleated. In addition, in the environment with relatively abundant super-cooled water, the Bergeron and collision-coalescence processes are accelerated, which favors the formation of large-size precipitation particles. Therefore, the particle spectrum was broadened, leading to different falling velocities of particles and a significant broadening of the velocity spectrum. As for the CFADs of Doppler radar velocity, there was a broadening of the overall Doppler radar velocity range and a significant increase in the terminal velocities of precipitation particles. About 30 minutes after the seeding in the convective region, the median terminal velocity increases from 0.5 $m \cdot s^{-1}$ to 5.0 $m \cdot s^{-1}$ in the convective region and from 1.0 $m \cdot s^{-1}$ to 1.25 $m \cdot s^{-1}$ in the stratiform region.

4.2 Analysis of cloud microphysical properties from aircraft observations

The above analysis of airborne KPR data shows that the seeding operation over different parts of the mixed convective-stratiform clouds leads to different evolutions of cloud macro-physical characteristics. In this section, we focus on the evolutions of micro-physical characteristics after seeding in the convective parts of cloud and the stratiform parts of cloud. However, we should note that the aircraft did not pass through the convective core part for safety consideration. Instead, it went through the upper part of the convective region and made the measurements of cloud microphysical properties there. This would result in relatively low liquid water content and small droplet number concentration over the convective region. Thus, the analysis here mainly focuses on the evolutions of micro-physical characteristics after seeding over two regions, rather than their comparisons.

As shown in Figs. 7a–7c, before the seeding, the convective cloud during S1–S3 and the stratiform cloud during S4–S6 were mainly composed of super-cooled droplets. Specifically, the average diameter from the CDP was 7.4 μm during the period S1–S3, and the liquid water content (LWC) was 0.04 $g \cdot m^{-3}$, with a concentration of 25.5 cm^{-3}. During S4–S6, the average diameter from the CDP was 7.5 μm, and the LWC was 0.09 $g \cdot m^{-3}$, with a concentration of 79.6 cm^{-3}. The CIP concentrations were lower in both cloud regions, and the ice water contents (IWC) were also lower (4.0×10^{-6} and 5.7×10^{-5} $g \cdot m^{-3}$, respectively). The diameters of graupel particles and dendritic snow crystals in the stratiform cloud were larger than those in the convective cloud. After the seeding operation, the mean concentration, diameter and LWC from the CDP in both regions decreased significantly. In contrast, the mean concentration and diameter from the CIP and the IWC increased significantly. Therefore, snow crystals and droplets with diameters above 300 μm appeared, and the PIP concentration also increased by one order of magnitude. The CIP in Fig. 7d shows that the cloud was mainly composed of graupel particles and columnar ice crystals before the seeding. While after the seeding, it was noted that on the ice crystal surface there was a gas-phase riming process to form dendritic snow crystals, causing the coexistence of ice crystals and rimed snow crystals.

For the convective cloud during S1–S3, Fig. 8 shows that the mean concentrations from the CDP, CIP and PIP changed from 212.8 $L^{-1}.\mu m^{-1}$, 0.017 $L^{-1}.\mu m^{-1}$ and 1.04×10^{-6} $L^{-1}.\mu m^{-1}$ to 139.2 $L^{-1}.\mu m^{-1}$, 0.005 $L^{-1}.\mu m^{-1}$ and 1.64×10^{-4} $L^{-1}.\mu m^{-1}$ after the seeding operation, respectively. The particle size from the CDP peaked at 5.5 μm both before and after the seeding; and the size of large-size cloud particles, i.e., the particle size recorded by the CIP, increased with maximum value changing from 225 μm to 1250 μm after the seeding. Moreover, the maximum precipitation particle size increased from 400 μm to maximum measurable size, 6200 μm. For the stratiform cloud during S4–S6, the mean concentrations from the CDP, CIP and PIP changed from 561.7 $L^{-1}.\mu m^{-1}$, 0.09 $L^{-1}.\mu m^{-1}$ and 1.0×10^{-8} $L^{-1}.\mu m^{-1}$ to 210.5 $L^{-1}.\mu m^{-1}$, 0.05 $L^{-1}.\mu m^{-1}$ and 3.57×10^{-4} $L^{-1}.\mu m^{-1}$ after the seeding, respectively. In addition, the maximum precipitation particle size increased from 700 μm to 5700 μm. The concentrations from the CDP and CIP decreased significantly after two seeding operations. However, the PIP concentration increased by 2–4 orders of magnitude, and its maximum particle size increased by 8–15 times. Together with Fig. 7d, it can be found that there are deposition processes to form dendritic snow crystals on the surface of ice crystals. It suggests that after seeding the AgI, the transformation of water from liquid to ice phase was accelerated, and the transformation was quite efficient. Note that the aircraft observation locations during S1–S3 are about 1–2 km above the convective core, which cannot represent the convective cloud properties reliably, thus the differences in cloud microphysical properties measured by aircraft between regions S1–S3 and S4–S6 cannot indicate anything about cloud response differences between convective and stratiform parts. Instead, as indicated earlier, the information from aircraft is mainly used for investigation of temporal evolution of cloud properties by seeding. The differences between Figs. 6a and 6b show that the upward Doppler velocity at the height of 1.0–4.5 km in the convective cloud increased from 0–0.5 $m \cdot s^{-1}$ to 3–5 $m \cdot s^{-1}$. The larger upward velocity favors the upward transport and condensation of water vapor. During this process, updrafts may also carry the AgI to higher levels where there are lower temperature, greater supersaturation and greater super-cooled water content. Note that the latent heat released by the deposition of supercooled water enhances the convective cloud development further because this heat release can lead to stronger updrafts and higher cloud tops. These factors accelerate the Bergeron and collision-coalescence processes to form large-size precipitation particles after seeding of the AgI, thereby increasing the precipitation (Simpson et.al., 1971; Sax et al., 1979; Woodley et al., 1982; Rosenfeld et.al., 1989; Bruintjes, 1999).

4.3 Evolution of seeding-producing ice monitored by satellites

(1) Analysis of NPP observations

To analyze the characteristics of the microphysical structure of cloud tracks in detail, the high resolution data from the NPP/Visible Infrared Imaging Radiometer Suite sensor at 05:25 UTC on 21 May 2018 are processed based on microphysical principles (Figs. 9a–9b). The flight tracks are colored in green, superimposed on the surrounding super-cooled water cloud which was shaded in yellow and orange. Figs. 9a–9b show that there was a clear cloud seeding track (referred to as the cloud track) on the cloud top along a line (around the dashed line in Fig. 9c) which is almost parallel to the section C-D in the flight track, and the cloud track extended about 15 km away from point C. Actually, the dashed line in Fig. 9c is around the location where section C–D moved to after 28–7 minutes of cloud seeding when the satellite passed by. The visible channel in Fig. 9b shows a southwest-northeast oriented seeding track 15–20 km southeast of section C–D. It indicates that the super-cooled water in the cloud was at least partially glaciated into ice particles, and the cloud particles became larger and sank, thus lowering the cloud top. In Fig. 9a, the shallow depth in cross-section 4 and the almost zero depth in cross-section 2 may be caused by the veiling of newly-formed thin super-cooled water cloud with small particle size. Fig. 9c shows that the section C–D, which had moved along the wind direction of 300° at a speed of 11 m·s^{-1} for 7–28 minutes from the original positions, was just inside the cloud track during 04:58:42–05:09:04 UTC. This result was consistent with the above analysis. Moreover, the brightness temperature (TBB) during the period R1–R3 was significantly higher than that during the period R4–R6, indicating the strong convective activity in the convective cloud region.

(2) Analysis of the H8 satellite data

To track the evolution and movement of the cloud tops after the seeding operation, the high-resolution data from the H8 satellite are adopted for further examination. The 10-minute TBB at 12 μm channel from the H8 satellite (Fig. 10) shows that the convective clouds in section A–B became blocky after the seeding operation during 04:52–04:57 UTC, and the TBB gradually decreased (note that seeded "A–B section" moves downwind with time), indicating the stronger convective activity. The stratiform cloud in section C–D for seeding operation was located in the front of a large block of mixed convective-stratiform clouds during 04:58–05:09 UTC. About 15 minutes after the seeding, a seeding track with a width of 1–3 km appeared 10 km downstream the seeding layer. Another 7 minutes later, a cloud seeding track with a width of 3–5 km was found at locations about 15–20 km downstream the seeding layer and continued to move southeastward at 11 $m \cdot s^{-1}$ along the wind direction of 300°. At 05:50 UTC, the seeding track already moved out of the flight area. Moreover, the seeding track below section G–H became narrow after its formation, which is likely due to the diffusion of the water cloud near the seeded volume to the cloud track center. It is also likely associated with the coverage of the newly-formed thin super-cooled water cloud with quite small particle size.

To examine the evolution trend of the cloud seeding tracks more clearly, the every-10-minute moving-downstream trajectory of section C–D along the wind direction of 300° at 11 $m \cdot s^{-1}$ was calculated. Then, the TBB values at 12-μm channel from the H8 satellite for each moving trajectory were extracted, and the boxplot of the TBB values was further obtained, as shown in Fig. 11. The 50th percentile of the TBB values shows a gradually increasing trend with time with a linear fitting line of $TBB = 0.5068 \times \Delta T + 234.87$, where ΔT is the number of time intervals from 05:00 UTC with the interval being 10 minutes. Note that the correlation coefficient between the 50th percentile of TBB and ΔT was 0.87. The TBB had increased by 4.1 K until 06:00 UTC, which indicates that the seeding track became more and more obvious, along with significant increases in its width and depth. Besides, the TBB decreased slightly at 05:40 UTC, which was likely attributed to the coverage of the newly-formed thin super-cooled water cloud. This result was consistent with the conclusions above.

5. Conceptual model for seeding operations of the mixed convective-stratiform clouds

Based on the above analysis results, a conceptual model of the AgI seeding for mixed convective-stratiform clouds is proposed, as shown in Fig. 12. Before the seeding operation (Fig. 12a), there are few ice crystals but many small cloud droplets in the two parts. In addition, there is a strong updraft in the convective region, resulting in the appearance of convective core. After the seeding of AgI (Fig. 12b), the ice crystals, snow crystals and precipitation particles rapidly increase in both parts. Moreover, due to the potential dynamic seeding mechanisms, enhanced updraft appears near the convective core, leading to a significant enhancement of convections.

The model shows distinct responses of different parts in mixed convective-stratiform clouds to the seeding operation. Specifically, the convective region has more vigorous convective activities after the seeding operation, with significantly enhanced echoes and higher echo tops. In addition, the dynamic seeding mechanism may also be involved, favoring the growth of particle size and broader full-spectra. The concentration of precipitation particles is higher and thus more precipitation forms. In contrast, after the seeding of AgI in the stratiform region, the transformation between droplets and ice crystals is accelerated, causing the surrounding super-cooled water to condense into ice crystals. Subsequently, the ice crystals grow up and fall under the effects of the Bergeron and collision-coalescence processes. At that time, the echoes significantly weaken at heights within 2-3 km around the seeding layer, with the echo top lowered, and obvious icing seeding tracks with a hollow structure appeared. Eventually, large-size particles fall onto the ground as surface precipitation. In this process, the static seeding mechanism plays the crucial role.

6. Conclusion and discussion

In this study, based on observations from the airborne KPR, NPP satellite and high-resolution H8 satellite, the cloud macro- and micro-physical characteristics as well as responses to the seeding operation in the convective and stratiform regions for a mixed convective-stratiform cloud occurred in Shandong during spring are analyzed. The main conclusions are as follows.

Based on the in-situ aircraft (equipped with the KPR) observations, different physical responses to the seeding in the convective and stratiform regions of the mixed convective-stratiform clouds are tracked and investigated. In terms of the convective region, the radar echoes became stronger with a denser depth, and the echo top height increased by 0.5–1.0 km. The median *Ze* was 5–7 dBZ higher than that before the seeding, and the near-surface *Ze* increased to 28 dBZ from 12 dBZ. The concentrations from the CDP and CIP both decreased significantly. However, the PIP concentration increased by 2-4 orders of magnitude, and the maximum size of precipitation particles increased from 400 μm to 6200 μm by more than 15 times. It implies that the AgI seeding in the convective region accelerates the formation of large-size precipitation particles by the Bergeron, riming and collision-coalescence processes. In the stratiform region, there were obvious icing seeding tracks after the seeding operation. The echoes became significantly weaker at heights within about 2-3 km around the seeding layer, and the echo top height was lowered by 1.4–1.7 km. The median Ze was 2–3 dBZ lower than that before the seeding. In addition, a hollow structure of the echoes appeared within the height of 6.2–7.8 km, with the largest depth reaching about 1.6 km, a diameter of about 5.5 km and a duration of 1 hour. The size of precipitation particles increased from 700 μm to 5700 μm by more than 8 times. Moreover, there were gas-phase riming process to form dendritic snow crystals on the surface of ice crystals, causing the coexistence of ice crystals and rimed snow crystals. This phenomenon indicates that after seeding the AgI, the transformation between cloud and water was accelerated, which was quite complete and efficient.

The tracking and monitoring by the NPP and H8 satellites show that the convective clouds became blocky after the seeding. In addition, the TBB decreased, indicating stronger convective activities in the convective region. 15 minutes after seeding the AgI in the stratiform region, a cloud seeding track with a width of 1–3 km appeared 10 km downstream the seeding layer. Another 7 minutes later, a cloud seeding track with a width of 3–5 km appeared 15 km downstream the seeding layer, and moved southeastward at the speed of 11 $m \cdot s^{-1}$ along the wind direction of 300° for 1 hour.

Comparing the physical responses to the seeding in two regions, it is found that in the convective region there were significant upward Doppler radar velocities of 3–5 $m \cdot s^{-1}$ at the heights of 1.0–4.5 km, which are favorable for the upward transport and further condensation of the water vapor. Moreover, the updrafts of convections may also carry the AgI to higher levels where there are lower temperature, higher supersaturation and higher supercooled water content. Note that the latent heat released by the condensation of supercooled water should enhance the effect of seeding on the convective cloud further, because this heat release can lead to stronger updrafts and higher cloud tops. These factors may result in the formation of large-size precipitation particles by accelerating the effects of Bergeron and collision-coalescence processes after seeding the AgI, thereby increasing the precipitation. However, in the stratiform region, the static seeding mechanism played the dominant role. That is, the surrounding supercooled water condensed into ice crystals by seeding the AgI, and then through the deposition process the ice crystals grew up and fell onto the ground as surface precipitation.

A challenging question we should note is the relative contribution of cloud seeding and natural variability to the observed phenomenon after cloud seeding. In principle, it is almost impossible to answer from observational view since we do not have two same clouds to compare between with and without cloud seeding. Thus, we here have simply attributed the cloud property changes mostly to cloud seeding, which warrants further investigation in future with mesoscale weather model simulations.

Acknowledgments. This work was supported by the National Key Research and Development Project (Grant No. 2019YFA0606803 and 2016YFA0601704), the National Natural Science Foundation of China (Grant No. 41925022), the Innovation and Development Project of China Meteorological Administration (CXFZ2022J036), and the Science and Technology Development Fund of Hubei Meteorological Bureau (Grant No. 2017Y06, 2017Y07, 2016Y06, and 2019Y10). NOAA Data Service Network provided NPP satellite data, the H8 10-minute full-disc data was also provided by the Data Service website of NOAA, and Shiyan Meteorological Bureau in Hubei Province provided valuable radar observation data and ground real-time data. In addition, we thank Nanjing Hurricane Translation for reviewing the English language quality of this paper.

Data Availability Statement

The data used in this study are available in this link (https://pan.baidu.com/s/1wwwCLKjTGy_HxD XdQFJd4Q).

References:

Biondini, R., Simpson, J., and Woodley, W., 1977. Empirical predictors for natural and seeded rainfall in the Florida area cumulus experiment (FACE), 1970–1975. J. Appl. Meteor., 16585–16594.

Boe, B.A., Heimbach, J.A., Krauss, T.W., Xue, L.L., Chu, X., and McPartland, J.T., 2014. The dispersion of silver iodide particles from ground-based generators over complex terrain. Part I: Observations with acoustic ice nucleus counters. J. Appl. Meteor. Climatol., 53, 1325–1341.

Bruintjes, R.T., 1999. A review of cloud seeding experiments to enhance precipitation and some new prospects. Bull. Amer. Meteor. Soc., 80, 805–820.

Cai, Z.X., Zhou, Y.Q., and Cai, M., 2013. Analysis on comprehensive observation of artificial precipitation enhancement operation for a mixed convective-stratiform cloud. Plateau Meteorology, 32(5), 1460-1469 (In Chinese).

Dai, J., Yu, X., Rosenfeld, D., et al., 2006. Analysis of Staellite observed microphsical signatures of cloud seeding tracks in supercooled layer clouds. Acta Meteorological Sinica(In Chinese), 64(5), 622-630.

DeMott, P. J., 1997. Report to North Dakota Atmospheric Resource Board and Weather Modification Incorporated on tests of the ice nucleating ability of aerosols produced by the Lohse Airborne Generator. Colorado State University Department of Atmospheric Science Tech. Rep., 38 pp.

Dong, X., Zhao, C., Yang, Y., Wang, Y.,Sun, Y., and Fan, R. (2020). Distinct change of supercooled liquid cloud properties by aerosols from an aircraft - based seeding experiment. Earth and Space Science, 7, e2020EA001196.

French, J.R., Friedrichb, K., Tessendorfc, S.A., Rauber, R.M., Geerts, B., Rasmussen, R.M., Xue, L.L., Kunkel, M.L., and Blestrud, D.R., 2018. Precipitation formation from orographic cloud seeding. Proceedings of the National Academy of Sciences of the United States of America, 115(6), 1168–1173.

Gabriel, K.R., 1999. Ratio statistics for randomized experiments in precipitation stimulation. J. Appl. Meteor., 38, 290–301.

Hallet, J., 1981. Ice crystal evolution in Florida summer cumuli following AgI seeding. Preprints, Eighth Conference on Inadvertent and Planned Weather Modification, Reno, NV, Amer. Meteor. Soc., 114–115.

Heymsfield, A.J., Thompson, G., Morrison, H., Bansemer, A., Rasmussen, R.M., Minnis, P., Wang, Z.E., and Zhang, D.M., 2011. Formation and spread of aircraft-induced holes in clouds. Science, 333, 77–81.

Heymsfield, G.M., Tian, L., Li, L.H, McLinden, M., and Cervantes, J.I., 2013. Airborne radar observation of severe hailstorms: Implications for future spaceborne radar. Applied Meteorology and Climatology, 52, 1851-1868.

Hillger, D., Kopp, T., Lee, T., Lindsey, D., Seaman, C., Miller, S., Solbrig, J., Kidder, S., Bachmeier, S., Jasmin, T., and Rink T., 2013. First-light imagery from suomi NPP VIIRS. Bull Amer Meteor Soc., 94(7), 1019-1029.

Hobbs, P.V., Lyons, J.H., Locatelli, J.D., Biswas, K.R., Radke, L.F., Weiss, R.R., and Rangno, A.L., 1981. Radar detection of cloud-seeding effects. Science, 213, 1250–1252.

Jing, X., Geerts, B., and Friedrich, K., 2015. Dual-polarization radar data analysis of the impact of ground-based glaciogenic seeding on winter orographic clouds. Part I: Mostly stratiform clouds. Applied Meteorology and Climatology, 54, 1945–1970.

Jing X., and Geerts, B., 2015. Dual-Polarization Radar Data Analysis of the Impact of Ground-Based Glaciogenic Seeding on Winter Orographic Clouds. Part II: Convective Clouds. Applied Meteorology and Climatology, 54, 2099-2117.

Jing, X.Q., Geerts, B., and Boe, B., 2016. The extra-area effect of orographic cloud seeding: Observational evidence of precipitation enhancement downwind of the target mountain. J. Appl. Meteor. Climatol., 55, 1409–1424.

Langmuir, I., 1950. Control of precipitation from cumulus clouds by various seeding techniques. Science, 112, 35–41.

Lawson, R.P., Baker, B., Pilson, B., and Mo, Q., 2006. In situ observations of the microphysical properties of wave, cirrus, and anvil clouds. Part II: Cirrus clouds. Journal of the Atmospheric Sciences, 63(12), 3186–3203.

Lawson, R.P., Pilson, B., Baker, B., Mo, Q., Jensen, E., Pfister, L., and Bui, P., 2008. Aircraft measurements of microphysical properties of subvisible cirrus in the tropical tropopause layer. Atmospheric Chemistry and Physics, 8(6), 1609–1620.

Lawson, R.P., Woods, S., Jensen, E., Erfani, E., Gurganus, C., Gallagher, M., Connolly, P., Whiteway, J., Baran, A.J., May, P., Heymsfield, A., Schmitt, C.G., McFarquhar, G., Um, J., Protat, A., Bailey, M., Lance, S., Muehlbauer, A., Stith, J., Korolev, A., Toon, O.B., and Kramer, M., 2019. A review of ice particle shapes in cirrus formed in situ and in anvils. Journal of Geophysical Research:Atmospheres, 124, 10049-10090.

Lawson P.R., Woods S., and Morrison H., 2015. The Microphysics of ice and precipitation development in tropical cumulus clouds. Journal of Atmospheric Sciences, 72, 2429-2445.

Lance, S., 2012. Coincidence errors in a cloud droplet probe (CDP) and a cloud and aerosol spectrometer (CAS), and the improved performance of a modified CDP. Journal of Atmospheric and Oceanic Technology, 29(10), 1532–1541.

Lin, G., Geerts, B.,Wang, Z.E., Grasmick, C., Jing, X.Q., and Yang, J., 2019. Interations between a nocturnal MCS and the stable boundary layer as observed by an airborne compact raman lidar during PECAN. Monthly Weather Review, 147, 3169-3188.

Nirel, R., and Rosenfeld, D., 1995. Estimation of the effect of operational seeding on rain amounts in Israel. J. Appl. Meteor., 34, 2220–2229.

Orville, H.D., 1996. A review of cloud modeling in weather modification. Bull. Amer. Meteor. Soc., 77, 1535–1555.

Pazmany, A.L., and Haimov, S.J., 2018. Coherent power measurements with a compact airborne Ka-band precipitation radar. Journal of Atmospheric and Oceanic Technology,

35, 3-19.
Pokharel, B., Geerts, B., and Jing, X.Q., 2015. The impact of ground-based glaciogenic seeding on clouds and precipitation over mountains: A case study of a shallow orographic cloud with large supercooled droplets. J. Geophys. Res. Atmos., 120, 6056–6079.
Rosenfeld, D., and Woodley, W.L., 1989. Effects of cloud seeding in west Texas. J. Appl. Meteor., 28, 1050–1080.
Rosenfled, D., and Lensky, I.M., 1998. Satellite based insights into precipitation formation processes in continental and maritime convective clouds. Bull Meteor Soc., 79(11), 2457-2476.
Rosenfeld, D., Yu, X., and Dai J., 2005. Satellite-retrieved microstructure of AgI seeding tracks in supercooled layer clouds. Journal of Applied Meteorology, 44, 760-767.
Rosenfeld, D., Liu, G., Yu, X., Zhu, Y., Dai, J., Xu, X., and Yue, Z., 2014. High-resolution (375m) cloud microstructure as seen from the NPP/VIIRS satellite imager. Atmos. Chem. Phys., 14(5), 2479-2496.
Sax, R.I., Thomas, J., Bonebrake, M., and Hallett, J., 1979. Ice evolution within seeded and nonseeded Florida cumuli. J. Appl. Meteor., 18, 203–214.
Smith, E.J., 1949. Experiments in seeding cumuliform cloud layers with dry ice. Aust. J. Sci. Res., 2, 78–91.
Simpson, J., and Woodley, W.L., 1971. Seeding cumulus in Florida: New 1970 results. Science, 172, 117–126.
Silverman, B.A., 2001. A critical assessment of glaciogenic seeding of convective clouds for rainfall enhancement. Bull. Amer. Meteor. Soc., 82, 903–924.

Vonnegut, B., and Chessin, H., 1971. Ice nucleation by coprecipitated silver iodide and silver bromide. Science, 174, 945–946.

Woodley, W.L., Jordan, J., Simpson, J., Biondini, R., and Flueck, J., 1982. Rainfall results of the Florida Area Cumulus Experiment, 1970–76. Journal of Applied Meteorology and Climatology, 21, 139–164.

Woodley, W.L., Rosenfeld, D., and Silverman, B.A., 2003. Results of on-top glaciogenic cloud seeding in Thailand. Part I: The demonstration experiment. Journal of Applied Meteorology and Climatology, 42, 920–938.

Woodley, W.L., and Rosenfeld, D., 2004. The development and testing of a new method to evaluate the operational cloudseeding programs in Texas. Journal of Applied Meteorology and Climatology, 43, 249–263.

Xue, L.L., Hashimoto, A., Murakami, M., Rusmussen, R., Tessendorf, S.A., Breed, D., Parkinson, S., Holbrook, P., and Blestrud, D., 2013. Implementation of a Silver Iodide Cloud-Seeding Parameterization in WRF. Part I: Model Description and Idealized 2D Sensitivity Tests. Journal of Applied Meteorology and Climatology, 52, 1433-1457.

Xue, L.L., Tessendorf, S.A., Nelson, E., Rasmussen, R., Breed, D., Parkinson, S., Holbrook, P., and Blestrud, D., 2013. Implementation of a Silver Iodide Cloud-Seeding Parameterization in WRF. Part II: 3D Simulations of Actual Seeding Events and Sensitivity Tests. Journal of Applied Meteorology and Climatology, 52, 1458-1476.

Xue, L.L, Chu, X., Rasmussen, R., Breed, D., Boe, B., and Greets, B., 2014. The dispersion of silver iodide particles from ground-based generators over complex terrain. Part II: WRF large-eddy simulations versus observations. Journal of Applied Meteorology and

Climatology, 53. 1342-1361.

Yang, J., Li, J., Li, P., Sun, G., Cai, Z., Yang, X., Cui, C., Dong, X., Xi, B., and Wan, R., 2020. Spatial distribution and impacts of aerosols on clouds under Meiyu frontal weather background over central China based on aircraft observations. Journal of Geophysical Research: Atmospheres, 125, e2019JD031915.

Yang, Y., Zhao C., Dong, X., Fan, G., Zhou, Y., Wang, Y., Zhao, L., Lv, F., and Yan, F., 2019. Toward understanding the process-level impacts of aerosols on microphysical properties of shallow cumulus cloud using aircraft observations, Atmospheric Research, 221, 27-33.

Yu, X., Dai, J., Lei, H.C., Xu, X., Fan, P., Chen, Z., Duan, C., and Wang, Y., 2005. Physical effect of AgI cloud seeding revealed by NOAA satellite imagery. Chinese Science Bulletin, 50, 44-51.

Zhao, C., Zhao, L., and Dong, X., 2019. A case study of stratus cloud properties using in situ aircraft observations over Huanghua, China, Atmosphere, 10(1), 19.

Figures

Figure 1. Photos of the KingAir aircraft probes, including AgI flares equipment, Ka-band cloud radar (KPR), cloud combination probe (CCP), cloud imaging probe (CIP), precipitation image probe (PIP), 20 Hz Aircraft-Integrated Meteorological Measurement System (AIMMS-20), Passive Cavity Aerosol Spectrometer Probe (PCASP), cloud condensation nuclei (CCN) counter and Hot-Wire Liquid Water Content Sensor (LWC-100).

Figure 2. Synoptic weather situation along with the surface meteorology observations on 21 May 2018. (a) Geopotential height at 500 hPa and the wind at 700 hPa at 00:00 UTC, with the thick purple lines representing the weak waves and red dotted lines representing warm/cold shear lines. (b) Surface map that shows weather conditions using the standard synoptic symbols and rainfall at 06:00 UTC. The turning points of the seeding track are denoted by the characters O–A–K, and O points marks Jinan Yaoqiang Airport. The seeding area was carried out along the magenta lines of the zigzagging flight track (A–G), and the other magenta lines (O–A and G–O) were the detection area.

Figure 3. (a) Region DEM and the aircraft flight track from 04:37 to 05:49 UTC on 21 October 2018. The colored line was the flight track, the black box was the location of Binzhou radar, and the letters A-I and red points are the flight turning points. Note that the magenta lines represent the parallel lines of system movement with winds for the period between forward and backward flight time. (b) The characteristics of flight height (black line), in-cloud (red dot), flight speed (light blue), temperature (blue lines), relative humidity (green line) parameters from 04:37 to 05:49 UTC. (c) Vertical cross-section of radar reflectivity along the aircraft flight track from 04:37 to 05:49 UTC measured by the ground radar at Binzhou. The blue line was the flight track.

Figure 4. Evolution characteristics of real-time airborne KPR radar echoes during (a) S1–S3, (b) R4–R6 (30–32 minutes after the seeding in S1–S3), (c) the whole detection period, (d) S4–S6, and (e) R1–R3 (22–24 minutes after the seeding in S4–S6). The positions pointed by the blue arrows are points S2 and S5 before the seeding operation, and the positions pointed by the red arrows are the points R5 and R2 after the seeding operation.

Figure 5. Evolutions for the CFADs of the radar reflectivity factors during (a) S1–S3, (b) R4–R6, (c) S4–S6 and (d) R1–R3. Green, black and purple dashed lines represent the 25th percentile, median and 75th percentile respectively, and the blue dashed line represents the freezing level and the red dashed line represents the seeding level.

Figure 6. Same as Fig. 5, but for the Doppler radar velocity. The positive velocity indicates downward motion and the negative velocity indicates upward motion.

Figure 7. Evolution of each microphysical variable at different operational time during the horizontal flight stage at 04:52:30-05:28:30 UTC. (a) LWC and IWC. (b) CDP, CIP, and PIP measured cloud particle concentration. (c) the particle size from CDP, CIP, and PIP. (d) CIP measured cloud particle image.

Figure 8. Cloud particle size spectra during (a) S1–S3 and R4–R6 in convective cloud, and during (b) S4–S6 and R1–R3 in stratiform cloud. The black line segments are the measurements during the seeding operation, and the blue segments during the detection period. The squares denote data from the CDP, from the CIP and triangles from the PIP.

Figure 9. S-NPP VIIRS microphysical seeding track over central China at 05:25 UTC on 21 Oct 2018. The aircraft flew eastward so that the seeding track becomes older from right to left. (a) The red color composite for the visible reflectance, green for the 3.7 μm reflectance,

and blue for the 10.8 μm brightness temperature. Note that the six blue lines except the one labeled with "4" represent the moving tracks of cloud parts seeded (at location 1–6 except 4) with winds; and the blue line labeled with "4" represents the flight track in which aircraft measured the response of cloud properties after seeding for locations between 4 and 5 and between A and B (such as S1–S6 as shown in panel c). (b) 0.6 μm reflectance. (c) TBB at 12-μm channel with black line for the flight track and blue dotted line for the flight track moved along the wind direction of 300° after 7–28 minutes from the original position A–H.

Figure 10. Evolution characteristics of the 10-minute TBB at 12-μm channel from H8 satellite during (a–h) 04:50–06:00 UTC. Blue dashed lines are the actual flight track, and letters A–K are turning points.

Figure 11. Evolution characteristics of the 10-minute TBB at 12 μm channel from H8 satellite extracted along the moving section C–D. The solid line inside the box represents the 50th percentile, the lower line was the 25th percentile, the upper line was the 75th percentile, the dotted line was the mean value, and the lower and upper whiskers denote the 10th and 90th percentiles, respectively.

Figure 12. Conceptual model of seeding AgI at different parts of the mixed convective-stratiform clouds. The left panel shows the situation before seeding, and the right panel shows that after seeding. Green solid line was the flight track, and black dashed line was the freezing level. Signs such as particle category and airflow are shown in the legend.

Tables

Table 1. The main instruments and their detection variables used in this study, along with the measurement ranges, spatio-temporal resolution and the particle size spectral bin resolution.

Figure 1. Photos of the KingAir aircraft probes, including AgI flares equipment, Ka-band cloud radar (KPR), cloud combination probe (CCP), cloud imaging probe (CIP), precipitation image probe (PIP), 20 Hz Aircraft-Integrated Meteorological Measurement System (AIMMS-20), Passive Cavity Aerosol Spectrometer Probe (PCASP), cloud condensation nuclei (CCN) counter and Hot-Wire Liquid Water Content Sensor (LWC-100).

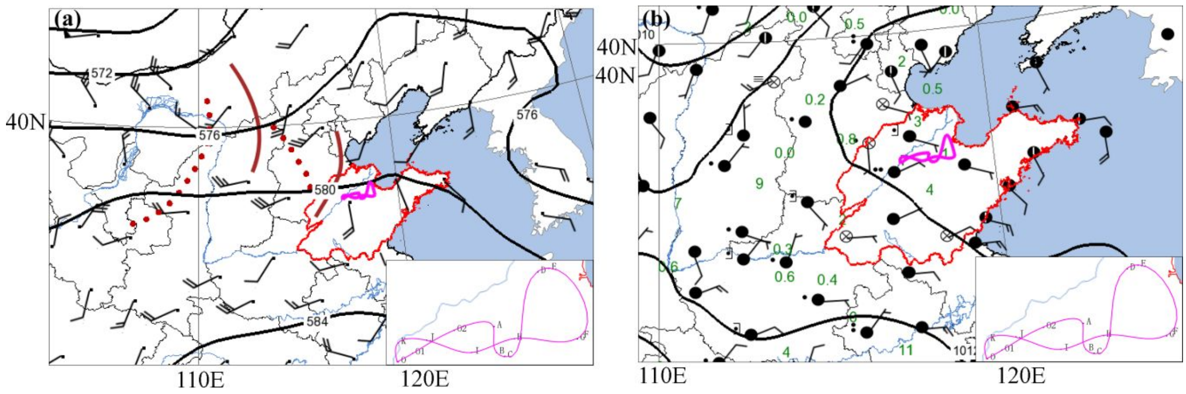

Figure 2. Synoptic weather situation along with the surface meteorology observations on 21 May 2018. (a) Geopotential height at 500 hPa and the wind at 700 hPa at 00:00 UTC, with the thick purple lines representing the weak waves and red dotted lines representing warm/cold shear lines. (b) Surface map that shows weather conditions using the standard synoptic symbols and rainfall at 06:00 UTC. The turning points of the seeding track are denoted by the characters O–A–K, and O points marks Jinan Yaoqiang Airport. The seeding area was carried out along the magenta lines of the zigzagging flight track (A–G), and the other magenta lines (O–A and G–O) were the detection area.

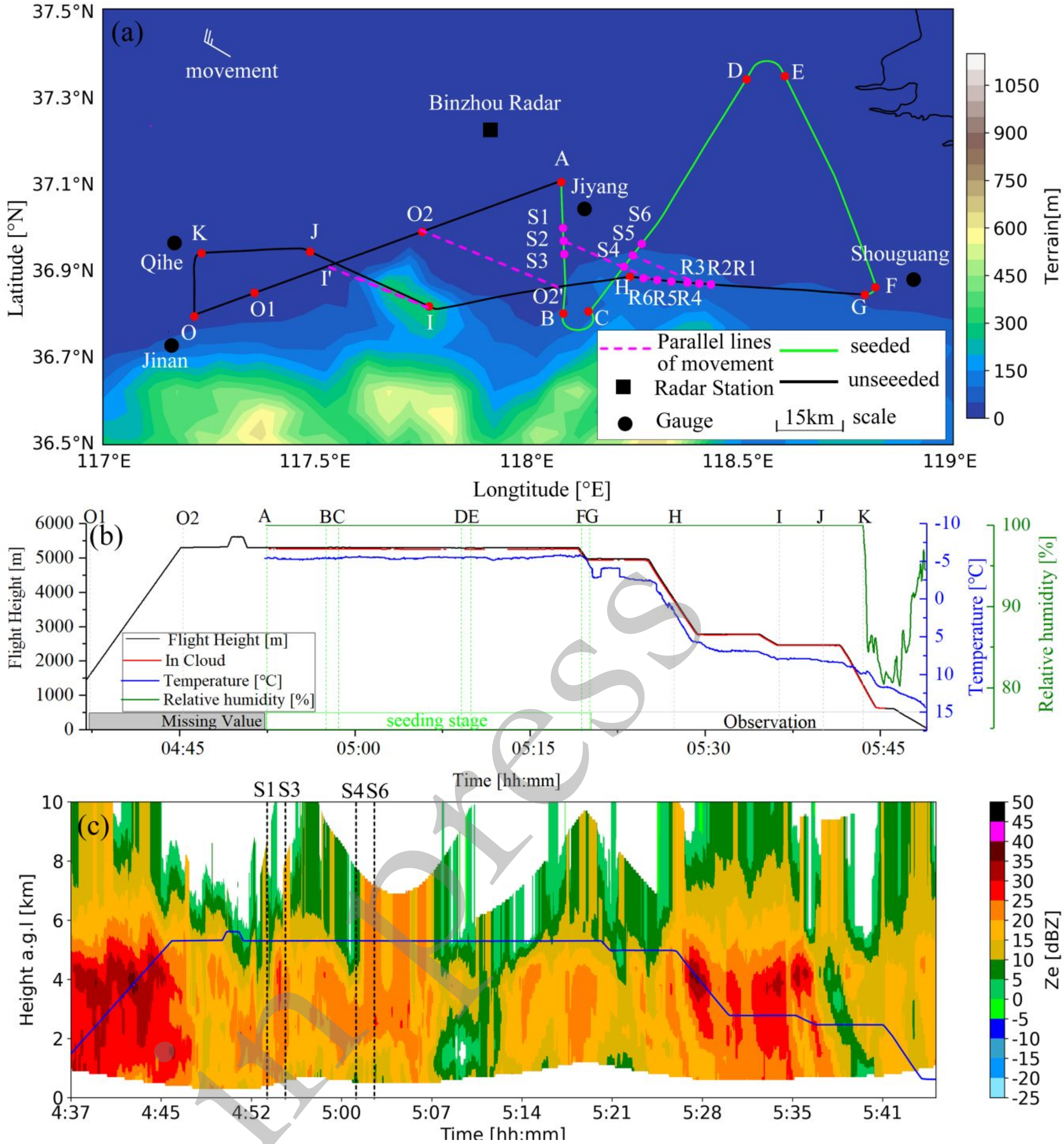

Figure 3. (a) Region DEM and the aircraft flight track from 04:37 to 05:49 UTC on 21 October 2018. The colored line was the flight track, the black box was the location of Binzhou radar, and the letters A–I and red points are the flight turning points. Note that the magenta lines represent the parallel lines of system movement with winds for the period between forward and backward flight time. (b) The characteristics of flight height (black line), in-cloud (red dot), flight speed (light blue), temperature (blue lines), relative humidity (green

line) parameters from 04:37 to 05:49 UTC. (c) Vertical cross-section of radar reflectivity along the aircraft flight track from 04:37 to 05:49 UTC measured by the ground radar at Binzhou. The blue line was the flight track.

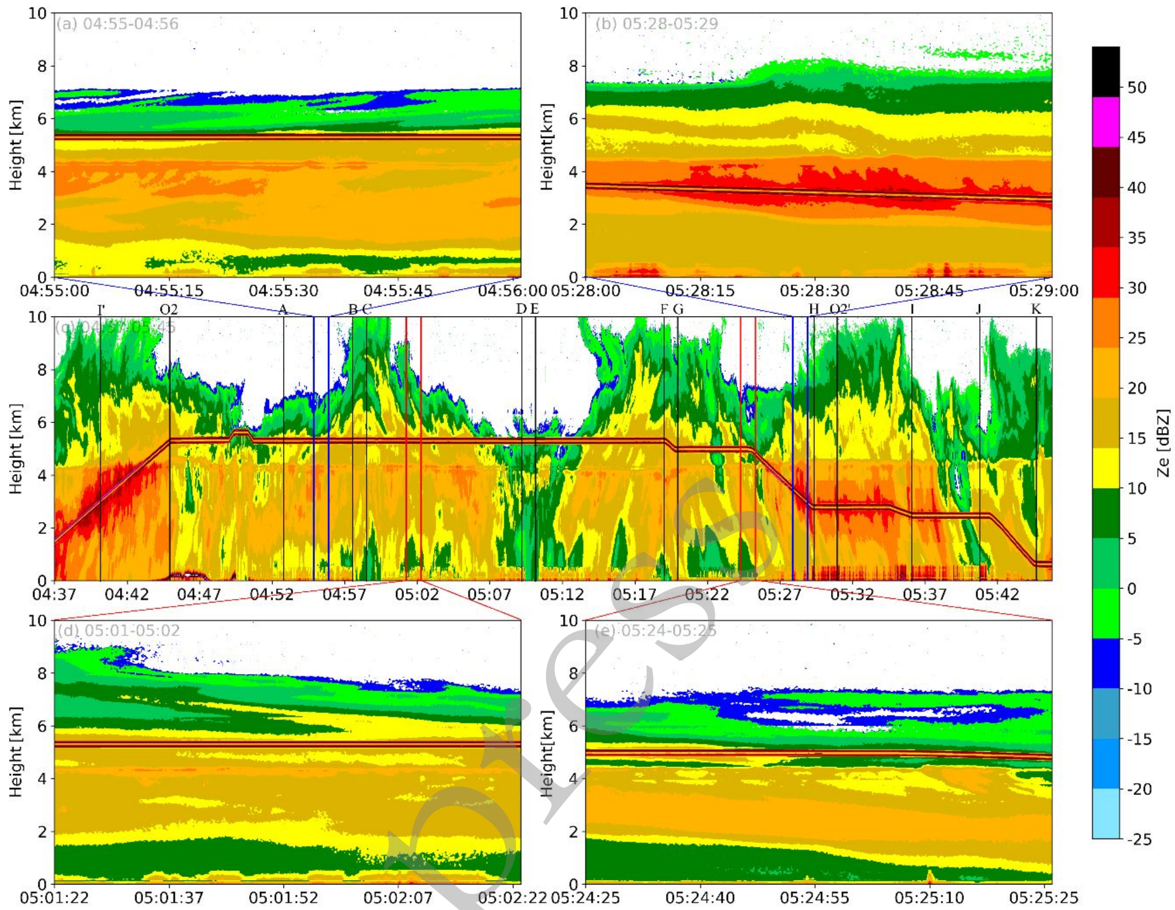

Figure 4. Evolution characteristics of real-time airborne KPR radar echoes during (a) S1–S3, (b) R4–R6 (30–32 minutes after the seeding in S1–S3), (c) the whole detection period, (d) S4–S6, and (e) R1–R3 (22–24 minutes after the seeding in S4–S6). The positions pointed by the blue arrows are points S2 and S5 before the seeding operation, and the positions pointed by the red arrows are the points R5 and R2 after the seeding operation.

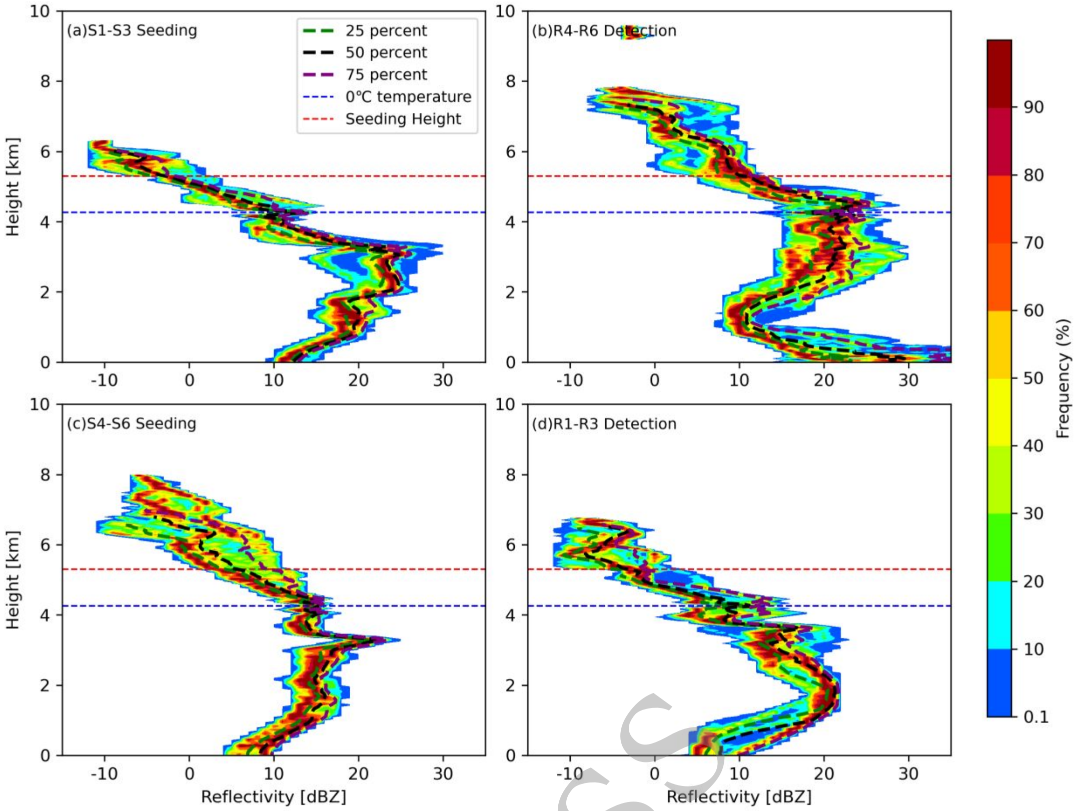

Figure 5. Evolutions for the CFADs of the radar reflectivity factors during (a) S1–S3, (b) R4–R6, (c) S4–S6 and (d) R1–R3. Green, black and purple dashed lines represent the 25th percentile, median and 75th percentile respectively, and the blue dashed line represents the freezing level and the red dashed line represents the seeding level.

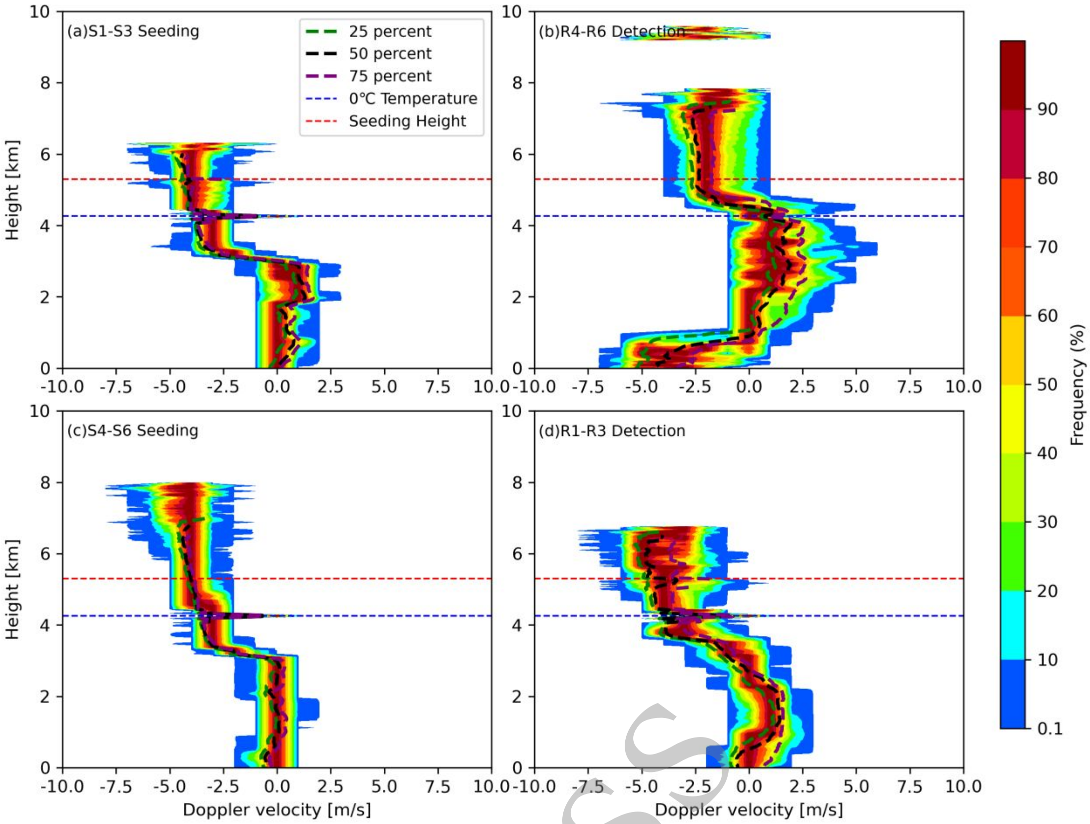

Figure 6. Same as Fig. 5, but for the Doppler radar velocity. The positive velocity indicates downward motion and the negative velocity indicates upward motion.

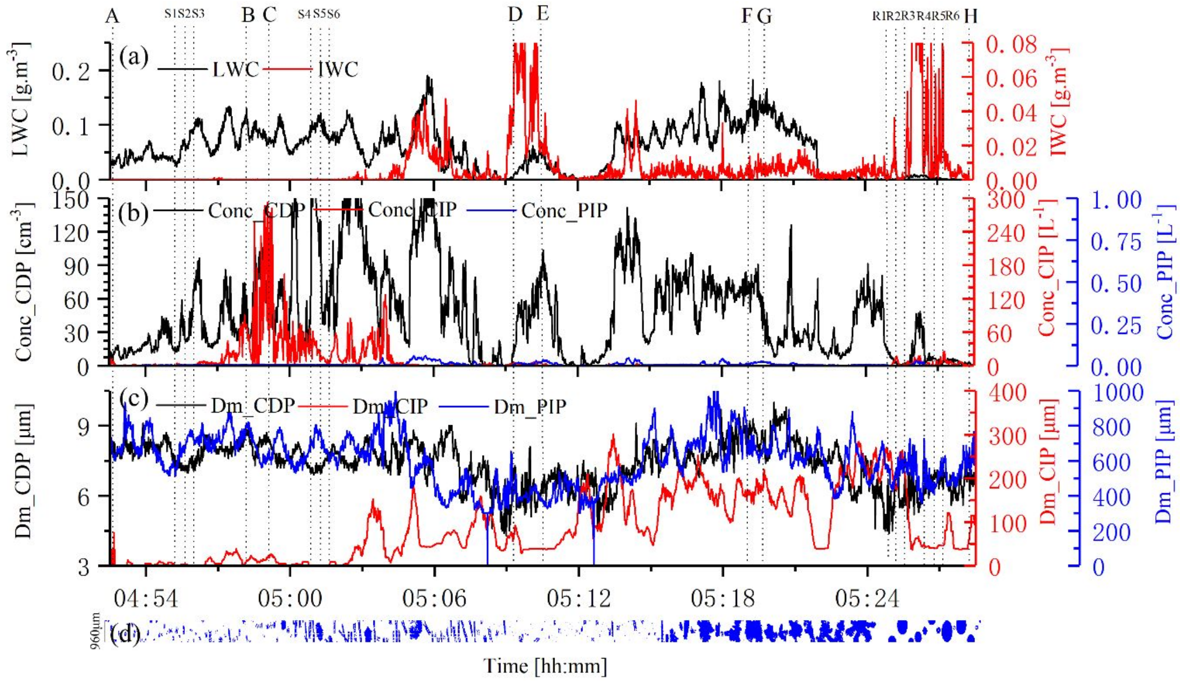

Figure 7. Evolution of each microphysical variable at different operational time during the horizontal flight stage at 04:52:30-05:28:30 UTC. (a) LWC and IWC. (b) CDP, CIP, and PIP measured cloud particle concentration. (c) the particle size from CDP, CIP, and PIP. (d) CIP measured cloud particle image.

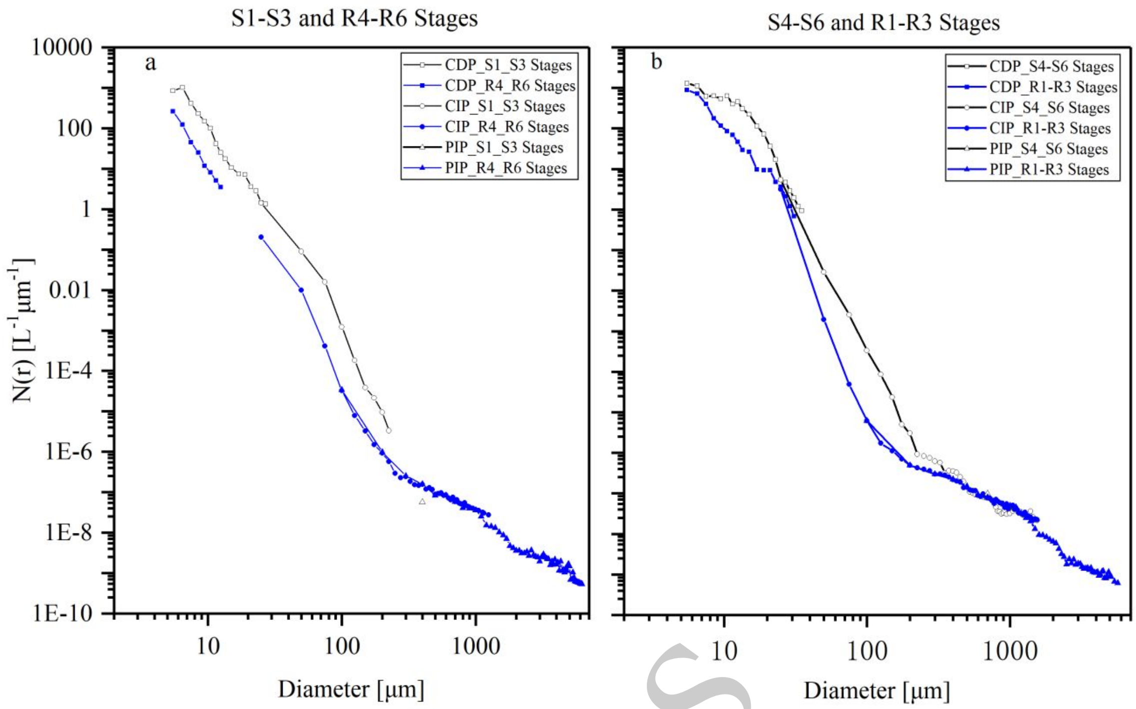

Figure 8. Cloud particle size spectra during (a) S1–S3 and R4–R6 in convective cloud, and during (b) S4–S6 and R1–R3 in stratiform cloud. The black line segments are the measurements during the seeding operation, and the blue segments during the detection period. The squares denote data from the CDP, from the CIP and triangles from the PIP.

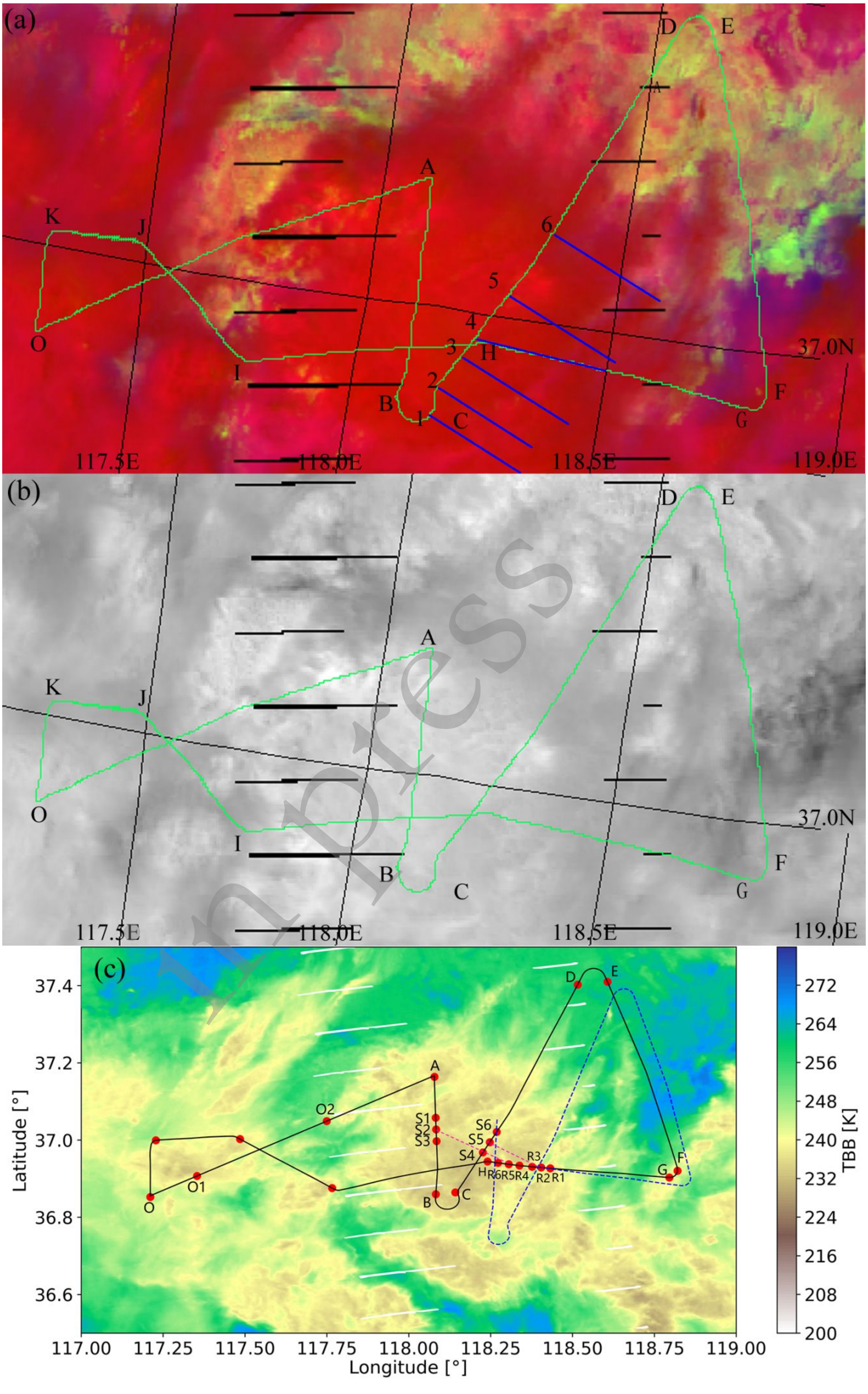
(a)
(b)
(c)
A
B
C
D
E
F
G
H
I
J
K
O
1
2
3
4
5
6
117.5E
118.0E
118.5E
119.0E
37.0N
O1
O2
S1
S2
S3
S4
S5
S6
R1
R2
R3
R4
R5
R6
37.4
37.2
37.0
36.8
36.6
Latitude [°]
117.00
117.25
117.50
117.75
118.00
118.25
118.50
118.75
119.00
Longitude [°]
272
264
256
248
240
232
224
216
208
200
TBB [K]

Figure 9. S-NPP VIIRS microphysical seeding track over central China at 05:25 UTC on 21 Oct 2018. The aircraft flew eastward so that the seeding track becomes older from right to left. (a) The red color composite for the visible reflectance, green for the 3.7 μm reflectance, and blue for the 10.8 μm brightness temperature. Note that the six blue lines except the one labeled with “4” represent the moving tracks of cloud parts seeded (at location 1–6 except 4) with winds; and the blue line labeled with “4” represents the flight track in which aircraft measured the response of cloud properties after seeding for locations between 4 and 5 and between A and B (such as S1–S6 as shown in panel c). (b) 0.6 μm reflectance. (c) TBB at 12-μm channel with black line for the flight track and blue dotted line for the flight track moved along the wind direction of 300° after 7–28 minutes from the original position A–H.

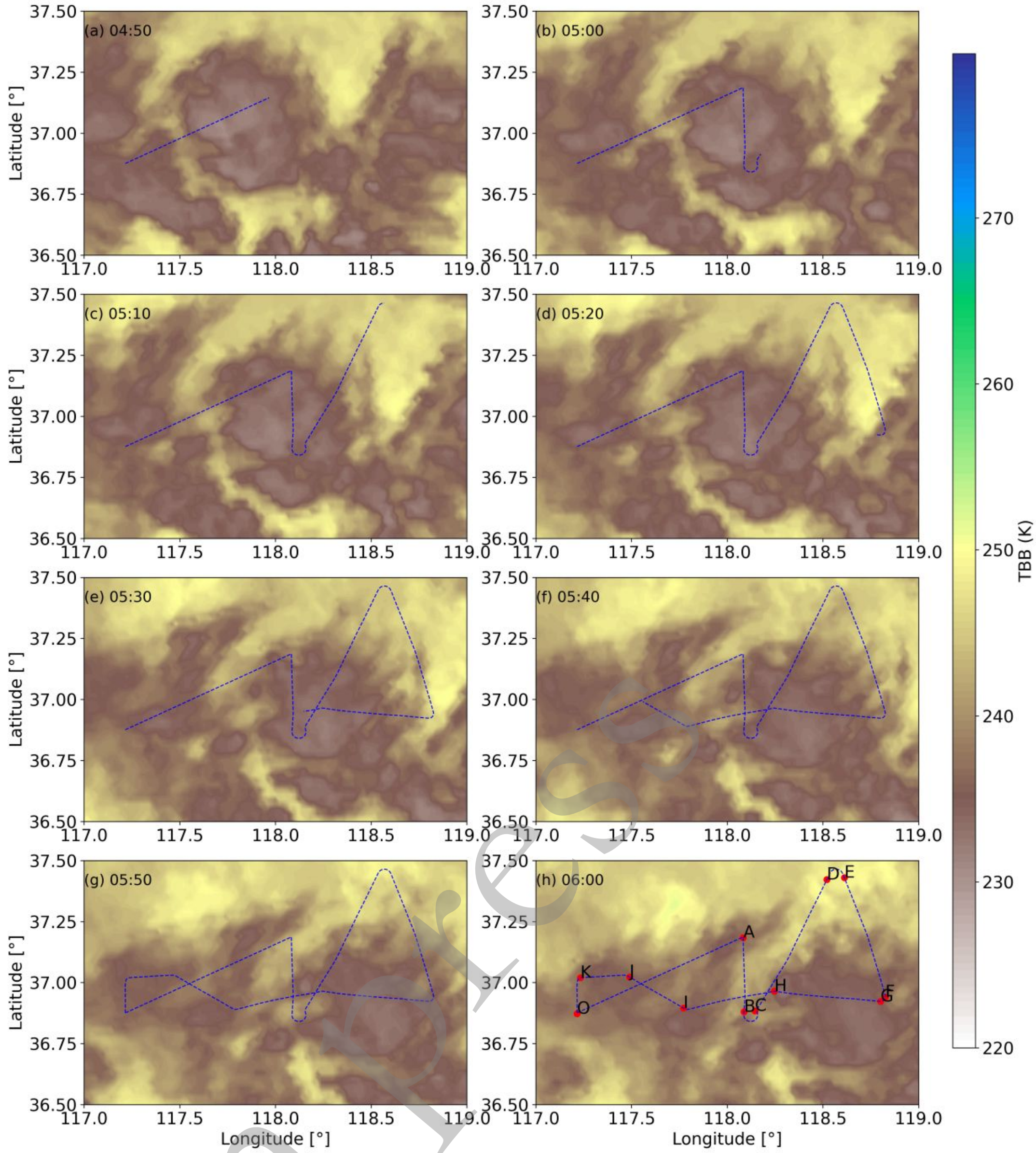

Figure 10. Evolution characteristics of the 10-minute TBB at 12-μm channel from H8 satellite during (a–h) 04:50–06:00 UTC. Blue dashed lines are the actual flight track, and letters A–K are turning points.

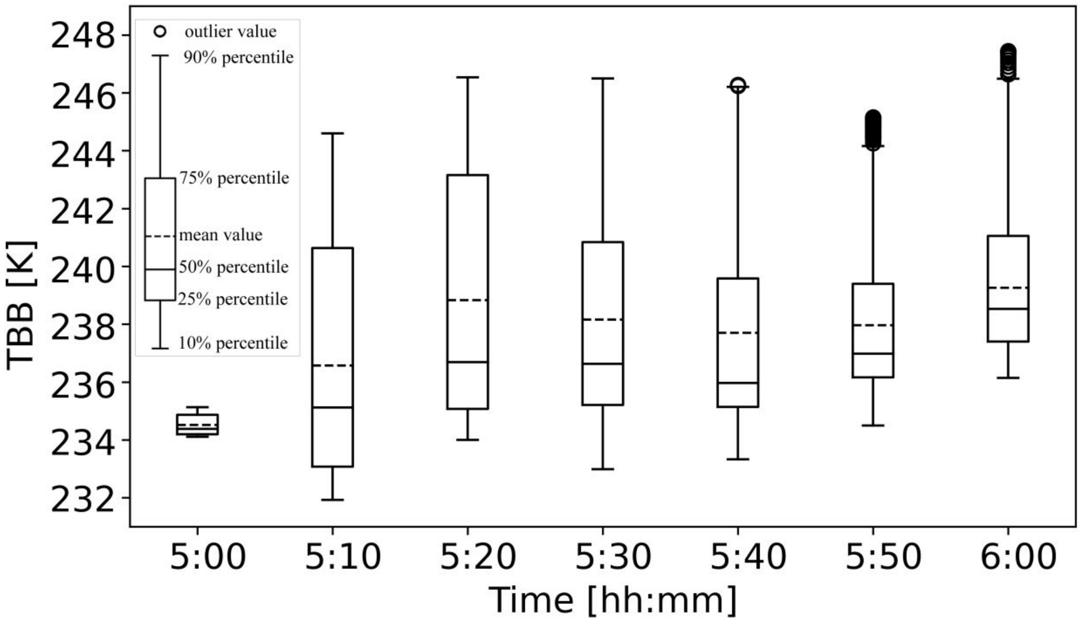

Figure 11. Evolution characteristics of the 10-minute TBB at 12 μm channel from H8 satellite extracted along the moving section C–D. The solid line inside the box represents the 50th percentile, the lower line was the 25th percentile, the upper line was the 75th percentile, the dotted line was the mean value, and the lower and upper whiskers denote the 10th and 90th percentiles, respectively.

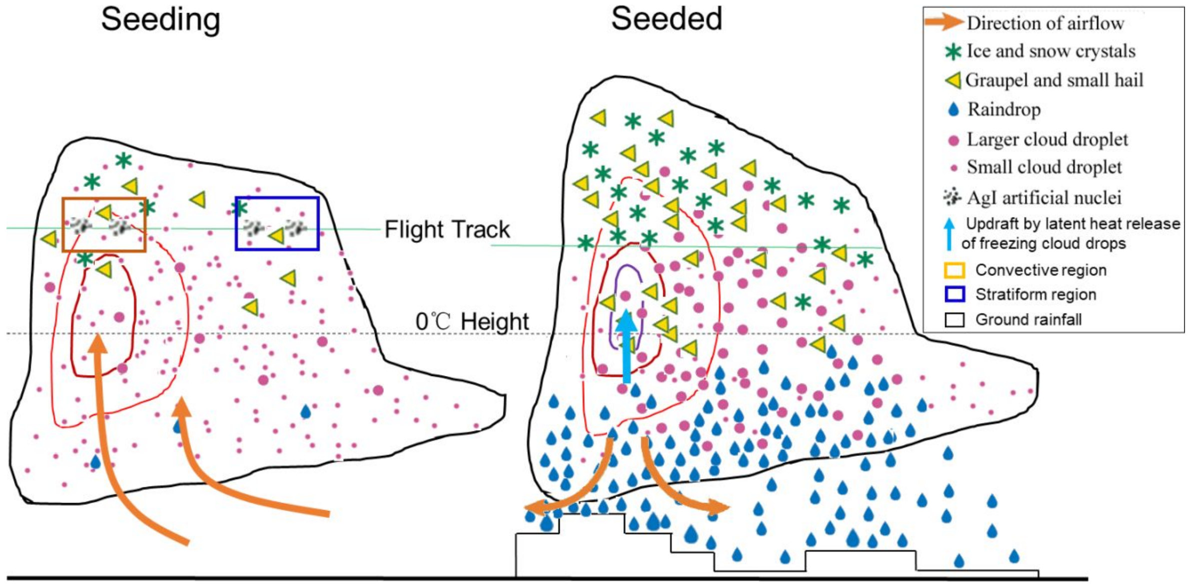

Figure 12. Conceptual model of seeding AgI at different parts of the mixed convective-stratiform clouds. The left panel shows the situation before seeding, and the right panel shows that after seeding. Green solid line was the flight track, and black dashed line was the freezing level. Signs such as particle category and airflow are shown in the legend.

Table 1. The main instruments and their detection variables used in this study, along with the measurement ranges, spatio-temporal resolution and the particle size spectral bin resolution.

Instrument	Variables detected	Measurement range	Resolution
Airborne Ka-band Radar (KPR)	Reflectivity Radial velocity	-25-55dBz -21-21m/s	Spatial：30m； Time：0.2s
CDP	Droplet size distribution	2-50μm	1μm
CIP	Cloud particle image	25-1550μm	25μm
PIP	Precipitation particle image	100-6200μm	100μm
AIMMS-20	Meteorology (temperature, humidity, and wind)	-	-